PNAS RESEARCH ARTICLE | CHEMISTRY

The structural origin of the efficient photochromism in natural minerals

Pauline Colinet[a], Hannah Byron[b], Sami Vuori[b], Juha-Pekka Lehtiö[c], Pekka Laukkanen[c], Ludo Van Goethem[d], Mika Lastusaari[b,1], and Tangui Le Bahers[a,1]

Edited by Donald Truhlar, University of Minnesota, Minneapolis, MN; received February 10, 2022; accepted March 25, 2022

In this work, the main properties characterizing the photochromism of hackmanites, tugtupites, and scapolites (three aluminosilicate natural minerals) are reported and compared. These properties are the activation energy necessary to generate the color, the absorption spectrum of the colored form, and the bleaching energy characterizing the return to a color-less mineral. An innovative joined experimental and computational approach is used to give an atomistic perspective on the origin of these properties allowing to understanding the difference of color or the lower stability of the colored form of the scapolite. It appears that the stability of the colored form is due to an unusual motion of a sodium atom, made possible by the specific structure of this mineral family, to stabilize a trapped electron responsible of the coloration. This motion is larger for hackmanite and tugtupites compared to scapolite, explaining the larger stability of the trapped electron in the two first minerals compared to the last one.

photochromism | aluminosilicates | density functional theory | doping | UV-vis spectroscopy

Photochromic materials are attracting scientists not only because of the nice-looking change of color but mainly because these materials can find many applications in high-tech devices such as optical memories and optical switches (1–3). Up to now, molecular crystals are the most investigated route for developing photochromic materials (4–6). Even if less studied, some inorganic solids also present a photochromic behavior. These include thin film oxides (WO_3, MoO_3 …) (3, 7, 8) which typically have poorly reversible photochromism (3), rare-earth doped materials (e.g., $Ba_5(PO_4)_3Cl:Eu^{2+}$ and $BaMgSiO_4:Eu^{2+}$) (9), and other materials reviewed by Badour et al. (10) For the latter, the photochromism originates from a photo-induced electron transfer from the rare-earth ion to an oxygen vacancy, giving rise to a trapped electron, also called an F-center. It is interesting to note that most ceramic materials (e.g., $BaMgSiO_4$ and Sr_2SnO_4) can actually show photochromism without rare-earth doping but they often have worse coloring efficiency (11). Thus arises the question of the possibility to have a strongly photochromic material without a rare-earth element. Interestingly, along with existing promising ceramic materials, efficient reversible inorganic photochromes have been known to geologists for decades but they have almost never been investigated by chemists (12). These minerals are natural from the aluminosilicate family: hackmanite ($Na_8Si_6Al_6O_{24}Cl_2$) (13, 14), tugtupite ($Na_8Al_2Be_2Si_8O_{24}Cl_2$) (12), and scapolite ($[Na,Ca]_4Al_3Si_9O_{24}[Cl,CO_3]_2$) (12). Hackmanite is no longer accepted as official name by the International Mineralogical Association. However, for consistency with previous publications, we will still use it in this work. In terms of crystal structure, these three minerals possess a characteristic aluminosilicate cage (called β-cage) containing a sodium polyhedron (a tetrahedron for hackmanite and tugtupite and a square for scapolite) with a chlorine ion standing in its center (Fig. 1). Hackmanite has been, to some degree, investigated by chemists (13, 15, 16), proving that its synthesis and compositional tuning are accessible. On the contrary, tugtupite and scapolite have almost not been considered for their photochromic properties up to now probably due to their difficult synthesis even if some examples are reported (17, 18). In addition, photochromic synthetic tugtupite or scapolite has not been reported to date. Especially, tugtupite is also rare in natural form. Therefore, we compare these minerals using natural samples rather than artificial ones. These three minerals, while belonging to the same family, experience different properties in terms of colored form (Fig. 1), activation energy, and bleaching energy. In this work, we will provide the complete characterization of the photochromism in these three natural minerals based on experiments and excited state quantum chemical calculations, including crystal embedding effects. Beyond these characterizations, we will present a physicochemical interpretation of the origin of their different behavior. We will prove that the electronic state inversion responsible for the photochromic phenomenon is due to an unusually strong atomic relaxation for the

Significance

Natural photochromic minerals have been reported by geologists for decades. However, the understanding of the photochromism mechanism has a key question still unanswered: What in their structure gives rise to the photochromism's reversibility? By combining experimental and computational methods specifically developed to investigate this photochromism, this work provides the answer to this fundamental question. The specific crystal structure of these minerals allows an unusual motion of the sodium atoms stabilizing the electronic states associated to the colored forms. With a complete understanding of the photochromism mechanism in hand, it is now possible to design new families of stable and tunable photochromic inorganic materials-based devices.

Author affiliations: [a]ENSL, CNRS, UCBL, Laboratoire de Chimie UMR 5182, 69364 Lyon, France; [b]Department of Chemistry, University of Turku, FI-20014 Turku, Finland; [c]Department of Physics and Astronomy, University of Turku, FI-20014 Turku, Finland; and [d]Mineralogical Society of Antwerp, Boterlaarbaan 225, 2100 Deurne, Belgium

Author contributions: L.V.G., M.L., and T.L.B. designed research; P.C., H.B., S.V., J.-P.L., L.V.G., M.L., and T.L.B. performed research; P.C., H.B., S.V., J.-P.L., P.L., L.V.G., M.L., and T.L.B. analyzed data; and M.L. and T.L.B. wrote the paper.

The authors declare no competing interest.

This article is a PNAS Direct Submission.

[1]To whom correspondence may be addressed. Email: tangui.le_bahers@ens-lyon.fr or miklas@utu.fi.

This article contains supporting information online at http://www.pnas.org/lookup/suppl/doi:10.1073/pnas.2202487119/-/DCSupplemental.

Published June 2, 2022.

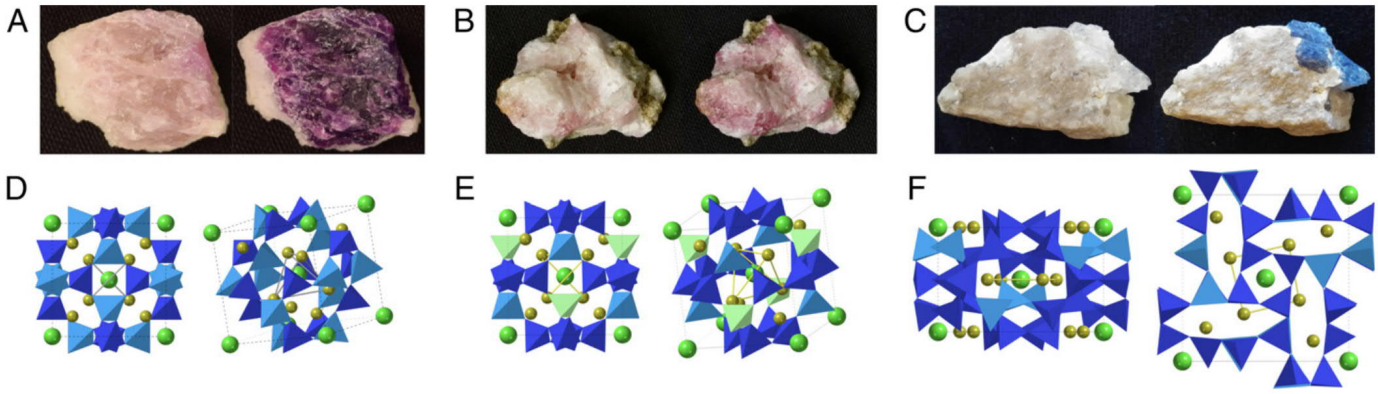

Fig. 1. Photos of the three materials in their colorless and colored forms. hackmanite (*A*), tugtupite (*B*), and scapolite (*C*). Different views of the three minerals' structure enhancing the characteristic β-cages made of silicate SiO_4^{4-} (blue), aluminate AlO_4^{5-} (cyan), and beryllate BeO_4^{6-} (mint green) corner-shared tetrahedra. Four sodium atoms (yellow) form a tetrahedron (hackmanite, *D*, and tugtupite, *E*) or a square (scapolite, *F*) in which lies a chloride atom (bright green).

inorganic solid state. This is made possible by the atomic organization offered by the crystal structures of these minerals based on the sodium polyhedron surrounded by the aluminosilicate β-cage.

Before starting, we may recall that in hackmanite, it is known that the photochromism originates from the substitution of a Cl^- by a S_2^{2-} ion generating at the same time a Cl^- vacancy in the adjacent β-cage, noted V_{Cl}, for charge neutrality (Eq. **1**) (15). Upon ultraviolet (UV) light exposure, the S_2^{2-} ion (called activator) transfers one of its electrons to V_{Cl} leading to a trapped electron called an F-center (Eq. **2**):

$$2Cl_{Cl}^- + S_2^{2-} \rightarrow (S_2)_{Cl}^{2-} + V_{Cl} + 2Cl^- \quad [1]$$

$$(S_2)_{Cl}^{2-} + V_{Cl} \rightleftarrows (S_2)_{Cl}^- + \mathbf{V_{Cl}^-}. \quad [2]$$

The electronic transitions of the F-center in the visible part of the spectrum are responsible for the color, while the return of the trapped electron on the disulfide anion corresponds to the bleaching of the material. Hence, the mineral can reversibly transition from a colorless to a colored form through an electron transfer. This working principle can be presented in energy levels on a reaction coordinate diagram (Fig. 2). The electron is initially localized on the S_2^{2-} ion giving the $^1[S_2^{2-},V_{Cl}(\mathbf{a_1})]$ ground state. The photo-induced activation corresponds to the population of the $\mathbf{a_1}$ orbital located on V_{Cl} ($^1[S_2^-,V_{Cl}(\mathbf{a_1})^-]$ excited state) followed by a spin relaxation to the triplet state ($^3[S_2^-,V_{Cl}(\mathbf{a_1})^-]$). The color corresponds to an electronic transition between the lowest orbital of V_{Cl}, $\mathbf{a_1}$, and the first unoccupied orbital of V_{Cl}, $\mathbf{t_2}$. The return of the electron from V_{Cl} to the sulfur impurity and the geometry relaxation associated corresponds to the bleaching of the material.

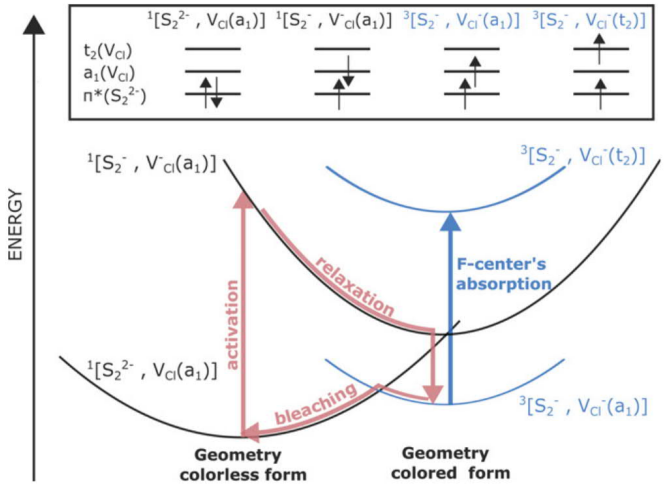

Fig. 2. Energy diagram representing the photochromism mechanism in aluminosilicate. The formation, relaxation and destruction of the F-center are depicted by red arrows. The blue arrow corresponds to the absorption of the F-center responsible of the color. Orbital descriptions of each electronic state are presented above the diagram.

Due to composition and crystal structure similarities between the three minerals considered in this article, it has been assumed that this photochromic mechanism is the same for all of them. However, analysis of the oxidation states of sulfur in these minerals typically reveals a large variety of sulfur-based species (19, 20), and we cannot rule out the possibility that the F-center can be generated from another sulfur impurity than S_2^{2-}. This will be investigated in the following by considering other sulfur impurities. Furthermore, while the fact that the photochromism originates from the inversion of the $^1[S_2^{2-},V_{Cl}(\mathbf{a_1})]$ and $^3[S_2^-,V_{Cl}(\mathbf{a_1})^-]$ states, leading to a metastable F-center, the reason why this state inversion is possible in these materials is still not described in the literature. We will highlight in this manuscript that an important "breathing" of the sodium polyhedron made possible by the large β-cages of these materials allows this state inversion.

By combining time-dependent density-functional theory (TD-DFT) computations and experimental characterizations especially designed for the investigation of photochromic minerals (e.g., thermotenebrescence), this article presents a deep analysis of the characteristics of this photochromism. The structure of the article will follow the mechanism of the photochromism starting by 1) the photo-induced electron transfer generating the F-center, then 2) the properties of the F-center, and finally 3) the bleaching of the material.

Results

In this work, the hackmanite and tugtupite originate from Greenland, while the scapolite is from Afghanistan. Structural and elemental analyses (see *SI Appendix*) confirm their respective crystallographic structure. The scapolite corresponds to a mineral family whose composition is between two crystallographic systems called marialite (formula $Na_4(Al_3Si_9O_{24})Cl$) and meionite (formula $Ca_4(Al_6Si_6O_{24})(CO_3)$) (21). The sample investigated here comprises 75% marialite and 25% meionite character based on the Na/Ca ratio. For simplicity, in quantum chemical calculations, the scapolite was modeled with a 100% marialite character. Since the marialite is by itself a solid solution, the interested readers will find out how we built this solid solution and the final structure we selected to model the

marialite in the *SI Appendix*. Briefly, in terms of experiments, we establish the energies associated with the creation of the color center, the absorption spectrum of the color center, as well as the thermal and optical bleaching of the color. Furthermore, we investigate the stability of the color center under regular room light and in the dark as well as the repeatability of the coloring-bleaching cycles (all data are in the *SI Appendix*). In terms of computational methodology, all geometries are obtained through periodic boundary conditions DFT calculations. Spectroscopic properties are then computed at the TD-DFT level on clusters extracted from the periodic geometries. These clusters are embedded in pseudopotentials and point charges fitted such as reproducing Madelung potential of the crystal (see computational details).

All the technical experimental and computational details are given in the *SI Appendix*.

Photochromism Activation. All three minerals show the characteristic orange photoluminescence (370 nm excitation) (*SI Appendix*, Fig. S4) of the S_2^- ion in the material as a signature of both the presence of sulfur-based impurities and the appropriate oxidation state of sulfur (17, 22, 23). However, only hackmanite and scapolite have a measurable quantity of sulfur (~0.2 at% for both) while tugtupite has no detectable S impurities by X-ray photoelectron spectroscopy (XPS), indicating that the S content is below 0.1 at%, corresponding to the limit of detection of the XPS (*SI Appendix*, Table S1). The excitation spectra associated with the coloration of the material is reported in Fig. 3 along with the TD-DFT computed charge transfer transition energies. The system is modeled by a sulfur-based impurity substituting a Cl atom in one β-cage and a Cl vacancy in the closest β-cage of the S-based impurity. The TD-DFT simulation involves a cluster made of the two β-cages surrounding the two defects (embedded in pseudopotentials and the fitted point charge array). For the three materials, the experimental spectrum is characterized by a broad band ranging from 375 nm (~3.3 eV) to 250 nm (~5.0 eV). The existence of shoulders (scapolite and hackmanites) indicates that several activators are probably responsible for the coloration. This is confirmed by computed activation energies when several sulfur-based activators are considered (SO_4^{2-}, SO_3^{2-}, S^{2-}, and S_2^{2-}). Interestingly, while the S_2^{2-} activator is generally considered to be the one responsible for the photochromism in artificial hackmanites, in natural aluminosilicates the activation energies computed with S^{2-} are also included in the experimental curves. Even SO_3^{2-} could be considered as an activator at high energy, but its activation energies are less in agreement with the experiment. The uncertainty of TD-DFT for the simulation of through space charge transfer transition does not allow us to clearly discriminate between the S_2^{2-} and S^{2-} as the main activator.

In other words, in natural minerals, several sulfur-based impurities can activate the photochromism, while in artificial ones for which the synthesis conditions are well defined, it may be possible to select the oxidation state of sulfur impurities and consequently the activation energy of the photochromism. From the measurements, it also appears possible to have several activators at the same time, enabling development of more complex applications.

Computed oscillator strengths associated to the photo-induced electron transfer are notably weak (between 10^{-4} and 10^{-2}), in agreement with the experimental observation that a longtime exposition under UV light is necessary to saturate the color (in the order of 10 min) (*SI Appendix*, Fig. S5). It must

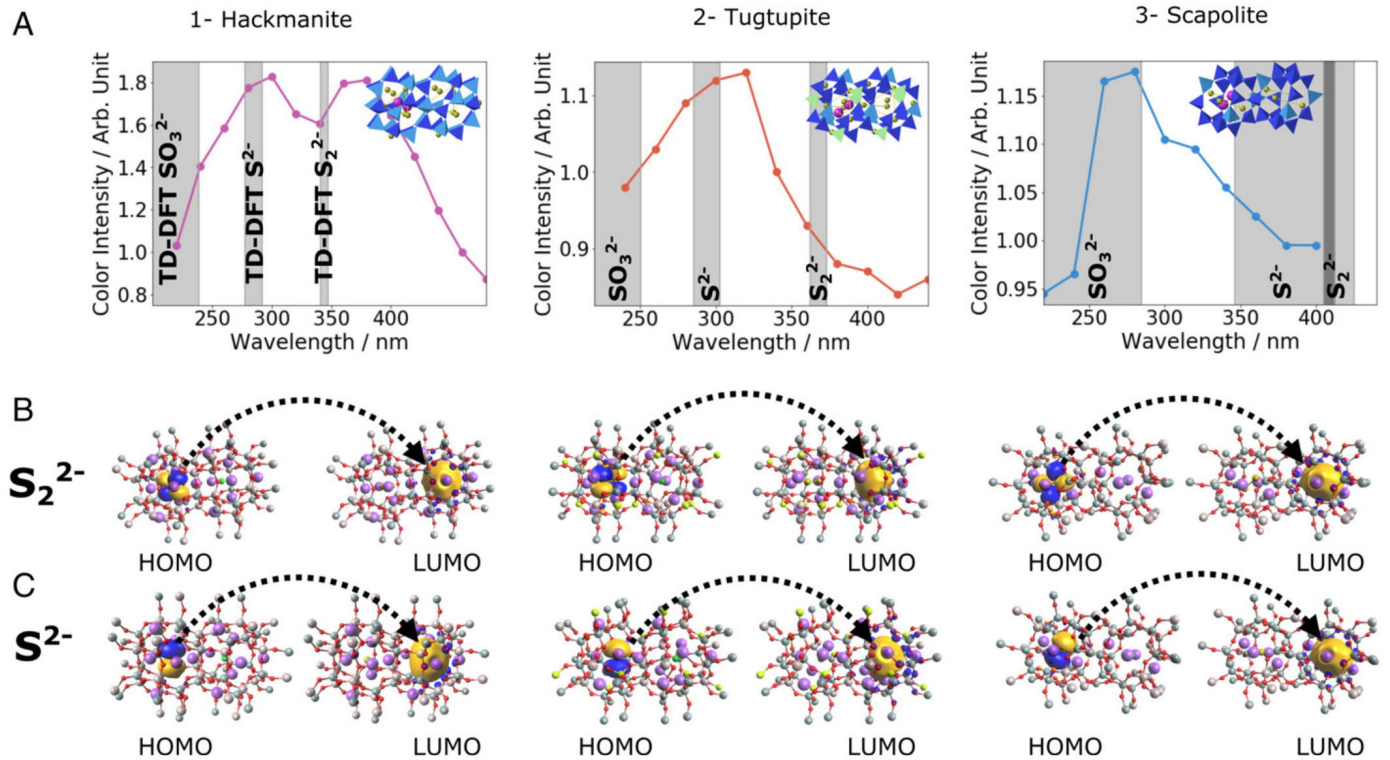

Fig. 3. Activation energy for the F-center formation. (*A*) Coloration excitation spectra of hackmanite, tugtupite and scapolite from left to right. The color intensity is given in arbitrary units. The 1.0 value reflects the moment the color is visible to the naked eye, the maximum of intensity cannot be compared between different materials. Vertical gray areas show the calculated excitation energy range by TD-DFT. The cluster used for the computation is represented on the top-right corner of each graph. (*B*) Representation of the extracted clusters along with the HOMO (π^*) and LUMO (a_1) orbitals involved in the transition for the activation of photochromism, when considering S_2^{2-} activator (isovalue 0.02 a.u.). The black dotted arrow depicts the electron transfer. (*C*) similar to (*B*) when considering S^{2-} activator, the HOMO is thus a 3p orbital.

be noted that the inherent compositional inhomogeneity of natural minerals results in multiple slightly different local structures around the sulfur-containing activators. This may cause some shifts and asymmetric broadening in all observed optical spectra.

The F-Center Absorption Spectrum. The most obvious difference between the three oxides considered in this work is the final color of the colored form (Figs. 1 and 4). These colors originate from the absorption spectrum of a trapped electron, presented in Fig. 4 in the form of reflectance spectra. The reflectance curves show broad minima centered at 550 nm (hackmanite), 510 nm (tugtupite), and 620 nm (scapolite). The nature of the color center is confirmed by TD-DFT calculations as an electron trapped in a chlorine vacancy with computed transitions at 500 nm (hackmanite), 490 nm (tugtupite), and 615 nm (scapolite). The shape and positions of the simulated reflectance spectrum agree with the experiment, ultimately leading to a simulated color close to the observed one. The orbitals of the trapped electron (Fig. 4) are delocalized beyond the Na_4 polyhedron explaining why a modification of the β-cage composition affects the transition energy of the F-center

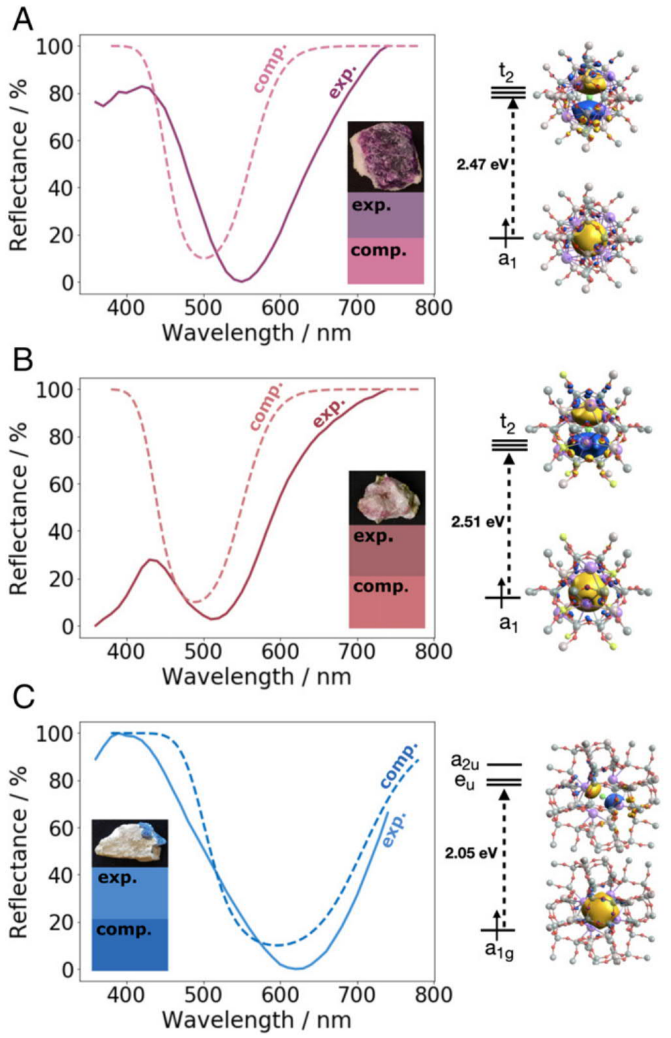

Fig. 4. Experimental (solid line) and simulated from TD-DFT (dotted line) reflectance spectra of (*A*) hackmanite, (*B*) tugtupite, and (*C*) scapolite. On the left part, experimental and simulated colors are given under a picture of the material. On the right part of each graph lies the representation of the orbitals involved in the absorption of the F-center (isovalue 0.02 a.u.). Orbital labels are associated to the point group of the Na_4 polyhedron (Td for hackmanite and tugtupite, D_{4h} for scapolite).

(when comparing hackmanite and tugtupite). The very different absorption spectrum of the scapolite (both experimentally and computationally) compared to the two other minerals highlights the large sensitivity of the F-center transitions with respect to the nature of the Na_4 polyhedron (a square for scapolite and a tetrahedron for the two other minerals). In a recent work, we also proved that the cell parameters also affect the energetics of this transition (22). In terms of transition intensity, the computed oscillator strengths are similar along the three minerals (~0.2). We can thus expect a close optical density in absorption for a similar F-center concentration and material properties (defect concentrations, surface roughness …) for the three aluminosilicates considered here.

Stability of the Colored Form: the Bleaching Energy. Once the F-center has been formed, questions of its relative stability (from a thermodynamic point of view) and its life-time (from a kinetic point of view) arise. As a first and simple observation, we note that at room temperature and under indoor light, the minerals return to a colorless form (in other words "bleach") with different kinetics: as an example of bleaching under 1600 lx white light, scapolite's color has a lifetime (time needed to drop to 1/e of the original intensity) of ~30 s, whereas for tugtupite the lifetime is 14 min and for hackmanite 20 min (*SI Appendix* and *SI Appendix*, Fig. S6). As a second observation, we note that after such optical bleaching, coloration and subsequent new bleaching can be carried out in repeated cycles (*SI Appendix*, Fig. S7). In darkness, where only the thermal energy available at room temperature affects the bleaching, the color lifetimes are 61 h for hackmanite and 66 h for tugtupite (*SI Appendix*, Fig. S8). However, both samples have still color left after 2 wk in darkness. Of course, it is impossible to actually measure color intensity in darkness and thus avoid the bleaching caused by the reflectance measurements themselves. Scapolite bleaches too fast to enable measuring any reasonable data in darkness.

The above is a first clue toward quite different electronic state energy profiles for the three minerals. To quantify the thermal activation energy associated to the bleaching, we set up a thermotenebrescence experiment (19) similar to the thermoluminescence experiments used to probe defect states in solids (see the *SI Appendix* for more information). The color intensity of the F-center is recorded upon a gradual temperature increase (3 °C/s) (*SI Appendix*, Fig. S9) allowing for the extraction of the thermal bleaching activation energies (0.28 eV, 0.72 eV, and 0.03 eV for hackmanite, tugtupite, and scapolite, respectively) and confirming the first rough observation.

To gain insight into the reason behind the metastability of the F-center at the atomic scale, we optimized the geometries of the colorless form (i.e., the minimum of the potential energy surface [PES] of the $^1[S_2^{2-},V_{Cl}]$ state corresponding to the electron on S_2^{2-}) and of the colored form (i.e., the minimum of the PES of the $^3[S_2^{-},V_{Cl}^{-}]$ state corresponding to the electron in Cl vacancy) at the DFT level using periodic boundary conditions. Looking at the structural changes between the colored and colorless, one can see that the shape and size of the β-cages are similar between the two forms, corresponding to the observation of Weller et al. (24) The main change occurs on the Na_4 polyhedron's shape and the dianion's bond length and orientation (Fig. 5*A*) with a contraction of Na_4 around the F-center (because the trapped electron attracts the surrounding Na^+ ions) and a decrease in S-S bond length in agreement with the depopulation of the π* anti-bonding orbital (Fig. 2) (15).

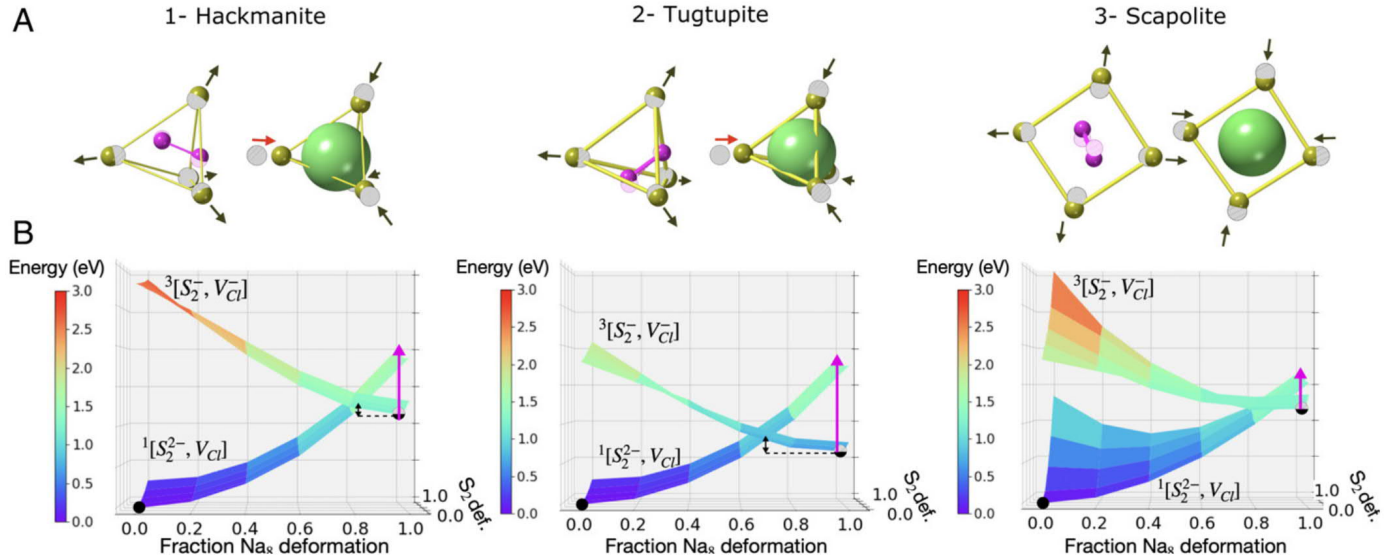

Fig. 5. Influence of the geometrical relaxation on the stabilization of the F-center. (*A*) Deformation of the two Na_4 polyhedra from the geometry of the colorless form (hatched atoms) to the geometry of the colored form. Dark arrows indicate the direction of deformation. Na are represented in yellow (or gray when hatched), sulfur in pink (hatched when in the geometry of the colorless form) and the trapped electron is depicted by a light green sphere. (*B*) Potential energy surfaces of the two states $^1[S_2^{2-},V_{Cl}]$ and $^3[S_2^-,V_{Cl}^-]$ with respect to the energy of $^1[S_2^{2-},V_{Cl}]$ at the geometry of the colorless form (0% deformation), as a function of the geometry deformation of S_2 and 2xNa_4. Stable geometries for the $^1[S_2^{2-},V_{Cl}]$ and $^3[S_2^-,V_{Cl}^-]$ states are presented by black points.

A scan of the PESs associated with the $^1[S_2^{2-},V_{Cl}]$ and $^3[S_2^-,V_{Cl}^-]$ states was computed (Fig. 5*B*) as a function of the sodium tetrahedra and S_2^{2-} deformations by DFT using a ΔSCF procedure in periodic boundary conditions. These scans indicate that the two PESs are mainly affected by the sodium polyhedron relaxations rather than the S-S contraction for the hackmanite and tugtupite while both motions contribute to the states' inversion for the scapolite.

A similar study was conducted considering S^{2-} as the activator. We optimized the geometries of the colorless form (i.e., the minimum of the PES of the $^1[S^{2-},V_{Cl}]$ state corresponding to the electron on S^{2-}) and of the colored form (i.e., the minimum of the PES of the $^3[S^-,V_{Cl}^-]$ state corresponding to the electron in Cl vacancy) at the DFT level using periodic boundary condition (PBC). This time, only the Na_4 polyhedron's deformation was considered (*SI Appendix*, Fig. S15*A*). A scan of the PESs associated with the $^1[S^{2-},V_{Cl}]$ and $^3[S^-,V_{Cl}^-]$ states was computed (*SI Appendix*, Fig. S15*B*) as a function of the sodium tetrahedra deformations by DFT in PBC. We observe again the inversion of the two states responsible for the photochromism phenomenon.

The color bleaching energy of these minerals can be extracted from the PES either as the vertical energy difference between the two states at the geometry of the colored form (i.e., the minimum energy of the $^3[S_2^-,V_{Cl}^-]$ state or $^3[S^-,V_{Cl}^-]$ state according to the activator), depicted by the pink arrow in Fig. 5*B*, or as the energy difference between the minimum energy of the $^3[S_2^-,V_{Cl}^-]$ (or $^3[S^-,V_{Cl}^-]$) state and the energy of the conical intersection, depicted by the black arrow in Fig. 5*B*. The vertical energy can also be computed by TD-DFT on a cluster extracted from the periodic system (see *SI Appendix*). All values are given in Table 1. Whatever the computational approach chosen, the trend obtained from theory is the same as the one obtained experimentally when considering S_2^{2-} activator. The F-center is the most stable in tugtupite followed by hackmanite then scapolite. This is not the case if S^{2-} is considered to be the activator leading to almost the same F-center stability for hackmanite and tugtupite (scapolite remaining much less stable). Considering the S^{2-} activator, the bleaching energy is smaller for scapolite, in agreement with the experimental observation, but the energies obtained for tugtupite and hackmanite are identical, if not higher for hackmanite (ΔSCF [conical]), which does correspond to the experimental order. This suggests that S_2^{2-} is most probably the main actor in the photochromism of these natural minerals, in agreement with the lower activation energy required to send an electron from this impurity toward the vacancy. Of note, we compute a positive bleaching energy by TD-DFT for the scapolite considering the S^{2-} ion as activator. In other words, TD-DFT does not predict any state inversion. Several reasons can explain this finding: first S^{2-} is maybe not the experimental activator; second, the crystal embedding is not well reproduced by point charges even if fitted to reproduce the

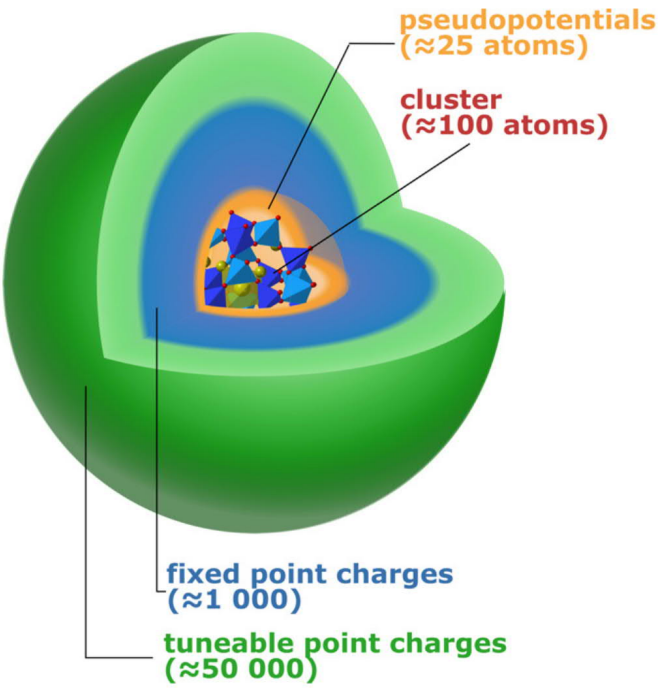

Fig. 6. Structure of the embedding used for the TD-DFT calculation.

Table 1. Experimental (from thermotenebrescence analysis) and computed (by ΔSCF on a periodic model or by TDDFT from a cluster approach) bleaching energies in eV

	Hackmanite	Tugtupite	Scapolite
Experimental	−0.28	−0.72	−0.03
Computed S_2^{2-}			
ΔSCF (vertical)	−0.88	−1.22	−0.44
ΔSCF (conical)	−0.12	−0.22	−0.01
TDDFT (vertical)	−0.38	−0.40	−0.26
Computed S^{2-}			
ΔSCF (vertical)	−0.96	−0.96	−0.67
ΔSCF (conical)	−0.23	−0.14	−0.09
TDDFT (vertical)	−0.19	−0.18	0.14

Madelung potential; and third, the through space character of the charge transfer transition is not well simulated by TD-DFT. It is not possible yet to find a good origin of the positive bleaching energy between these three reasons. Future developments in quantum chemical density embedding calculations (25) and in quantum chemistry (such as double hybrid functionals or GW/BSE) (26) will help to solve these problems.

Discussion

Molecular photochromic systems whose mechanisms are based on an important molecular reorganization, such as azo-benzene, are generally not adapted to experience the photochromism as a densely packed solid, as there is not enough free volume to allow such molecular motion. This limited geometrical relaxation in the solid state is also responsible for the difficulties in developing efficient reversible inorganic photochromism. From this perspective, the photochromic minerals presented in this work seem thus particularly unique. Quantum calculations bring the understanding of the origin of this stable and reversible photochromism. The structure of the aluminosilicate made of a β-cage surrounding a sodium polyhedron offers enough free space to allow a reversible "breathing" of the sodium polyhedron, ultimately leading to an inversion of two electronic states involved in the photochromic mechanism. As a matter of illustration, hackmanite and tugtupite experience a very large stabilization of the F-center (Table 1), much more than the scapolite. This is accomplished by a considerable motion of a specific sodium atom (presented by the red arrows in Fig. 5*A*), the one surrounding the F-center but pointing toward the activator (S_2^{2-} or S^{2-} ion) (Table 2). This atom moves by ∼1.2 Å to stabilize the F-center in hackmanite and tugtupite with an S_2^{2-} activator. In scapolite, this motion is only 0.6 Å because the two Na_4 squares surrounding the activator and V_{Cl} defects are far from each other. The same phenomenon is observed when considering S^{2-} activator, except in a larger extent (∼1.9 Å in hackmanite and tugtupite vs. 0.9 Å in scapolite) due to lower steric constraints.

Table 2. Largest sodium atom motions (in Å) surrounding the F-center but pointing toward the activator depending on both the activator and the mineral

	Hackmanite	Tugtupite	Scapolite
S_2^{2-}	1.33	1.07	0.60
S^{2-}	1.89	1.93	0.90

In the last few years, the facility to tune the composition of these minerals has been reported experimentally and computationally (19, 24, 27). While these works were done mainly to investigate the effect of composition on the final color of the F-center and almost only based on the hackmanite structure, we understand from the study presented here that all the characteristics associated with the photochromism of the aluminosilicate minerals can be controlled:

- The activation energy: by selecting the oxidation state of the sulfur activator by adapting the oxidoreduction condition during the synthesis or by using another alkaline ion instead of Na^+ (19);
- The F-center color: by selecting the appropriate Na_4 polyhedron (hackmanite, tugtupite vs. scapolite) and the composition of the β-cage (22); and
- The bleaching energy and the kinetic of the phenomenon: by modifying the flexibility of the Na_4 polyhedra first by selecting the structure (hackmanite, tugtupite vs. scapolite) then by tuning the β-cage volume upon chemical modifications.

Conclusions

The natural aluminosilicate minerals investigated here present unusually stable and reversible photochromism for inorganic materials. We proved that this phenomenon is due to an easy geometrical relaxation when going from the electronic state of the colorless form to the electronic state of the colored form (characterized by a trapped electron in a chlorine vacancy). This is not possible without the combination of the stable aluminosilicate β-cage and the space for movement within its voids. Surprisingly, while these minerals and their properties have been known by geologists for decades, only a very limited number of investigations have been published by solid state chemists. The information obtained in the present work shines light on the origin of the photochromism and on all the possibilities to tune the characteristic properties of this effect. Thus, there is no doubt that new families of inorganic photochromic materials with controllable properties are within reach.

Materials and Methods

Experimental Details. Crystal structure and purity were checked with X-ray powder diffraction measurements using a Huber G670 position sensitive detector and $CuK_{\alpha 1}$ radiation (λ = 1.54060 Å). Photoluminescence spectra were recorded with an Ocean Optics USB 2000+ spectrometer using a 365 nm LED for excitation. XPS measurements were carried out with Perkin-Elmer PHI 5400 ESCA system. Analysis of the XPS spectra was done with Origin 2016 program by removing Shirley background and fitting Voigt lineshapes to the spectra. The tenebrescence excitation spectra were compiled as follows: a white sample was partly irradiated with a Xe lamp (LOT-QuantumDesign LSB522, 150 W) for 5 min with each wavelength chosen with a LOT-QuantumDesign MSH300 monochromator. Then, the irradiated area's reflectance was measured with an Avantes HS-TEC spectrometer and Ocean Optics LS-1-Cal as the light source. The color intensity was obtained from integrating the visible wavelength range and subtracting the integral of a noncolored sample. After each excitation wavelength, the sample's color was bleached (500 nm, 5 min). For Fig. 4, the reflectance spectra were measured with a Konica Minolta CM-2300d spectrophotometer using D65 illuminant and 10° observer. Thermotenebrescence curves were constructed by following the reflectance (measured with an Avantes AvaSpec ULS2048CL-EVO spectrometer under an Ocean Optics LS-1 Cal calibration lamp directed toward the sample 20 cm away) of an initially fully colored (irradiated with UVP UVLS-24 operating with 4 W at 254 nm) sample as a function of

temperature. The heating was carried out using a MikroLab Thermoluminescent Materials Laboratory Reader RA'04 programmed at heating rate of 3 °C × s^{-1}. The signal was corrected for spontaneous fading and for effects in a noncolored sample's reflectance spectrum as a function of temperature to correct any discoloration effects induced by the heating. The thermal bleaching energies were obtained from these curves using the initial rise method (19). More information about the thermotenebrescence method is given in *SI Appendix*. The tenebrescence bleaching spectra were compiled with a similar procedure and setup as the tenebrescence excitation spectra described above. However, for the bleaching, the sample was first partially colored with a 5-min exposure to 254 nm UV radiation. Then, the sample was illuminated with the chosen wavelength for 5 min, and the reflectance spectrum was measured. The sample was re-irradiated (254 nm, 5 min) before proceeding to the next wavelength. These measurements were done at room temperature for hackmanite and tugtupite, whereas for scapolite, 77 K was used to minimize the effect of its fast thermally induced color bleaching.

Computational Details. All PBC calculations were performed within the DFT framework with the global hybrid functional PBE0 (28) along with the ab initio CRYSTAL17 code (29), using localized (Gaussian) basis sets and solving self-consistently the Hartree-Fock and Kohn-Sham equations thus allowing the efficient use of hybrid functionals. All-electron double-ζ basis sets with polarization functions were used for Si ([4s3p1d]/(20s12p1d)) (30), Al ([4s3p1d]/(17s9p1d)) (31), O ([3s2p1d]/(10s4p1d)) (32), and Cl ([4s3p1d]/(16s10p1d)) (33), while all-electron triple-ζ basis sets with polarization functions were used for Na ([4s3p1d]/(15s7p1d) (34). To describe the trapped electron, a basis set was optimized with the 111G(d) structure (optimized coefficients are given in the *SI Appendix*). The reciprocal space was sampled according to a sublattice with a 12 × 12 × 12 k-points mesh for the geometry optimization of the bulk system while a single k-point (the Γ point) was used for geometry optimization of the 2 × 2 × 2 supercell containing the defects. The convergence criterion for the SCF cycle was fixed at 10^{-7} Ha per unit cell.

TD-DFT was done using the Gaussian16 code (35) along with B3LYP (36–39) functional for the F-center absorption spectrum and CAM-B3LYP (40) functional for the computation of the charge transfer transitions (activation and bleaching energies). The quantum clusters contain the β-cages and the Na_4 polyhedra surrounding the impurities embedded in first shell of pseudopotentials at the positions of the closest Si^{4+}, Al^{3+} and Be^{2+} inside an array of point charges fitted to reproduce the Madelung potential of the crystal (22). Point charges used to simulate the Madelung potential of the crystal were obtained through the Ewald package (41–43). A 5 × 5 × 5 supercell was used to generate the point charges and the fitting procedure led to a root-mean-square error lower than 1 μV on the Ewald potential. The structure of this embedding is depicted in Fig. 6.

Data Availability. All study data are included in the article and/or supporting information.

ACKNOWLEDGMENTS. The authors thank the SYSPROD project and AXELERA Pôle de Compétitivité for financial support ("Pôle Scientifique de Modélisation Numérique" Data Center). This work was granted access to the high-performance computing resources of National Computing Center for Higher Education, "Institut du Développement et des Resources en Informatique Scientifique" (IDRIS), and "Très Grand Centre de Calcul" (TGCC) under the allocation 2018-080609 made by the "Grand Equipement National de Calcul Intensif" (GENCI). The authors acknowledge "Agence Nationale de la Recherche" (TeneMod project ANR-17-CE29-0007-21) for financial support.

1. J. Park, D. Feng, S. Yuan, H. C. Zhou, Photochromic metal-organic frameworks: Reversible control of singlet oxygen generation. *Angew. Chem. Int. Ed. Engl.* **54**, 430–435 (2015).
2. M. Irie, T. Fukaminato, K. Matsuda, S. Kobatake, Photochromism of diarylethene molecules and crystals: Memories, switches, and actuators. *Chem. Rev.* **114**, 12174–12277 (2014).
3. S. Wang, W. Fan, Z. Liu, A. Yu, X. Jiang, Advances on tungsten oxide based photochromic materials: Strategies to improve their photochromic properties. *J. Mater. Chem. C Mater. Opt. Electron. Devices* **6**, 191–212 (2018).
4. M. Irie, Photochromism of diarylethene single molecules and single crystals. *Photochem. Photobiol. Sci.* **9**, 1535–1542 (2010).
5. S. V. Paramonov, V. Lokshin, O. A. Fedorova, Spiropyran, chromene or spirooxazine ligands: Insights into mutual relations between complexing and photochromic properties. *J. Photochem. Photobiol. Chem.* **12**, 209–236 (2011).
6. D. Dattler *et al.*, Design of collective motions from synthetic molecular switches, rotors, and motors. *Chem. Rev.* **120**, 310–433 (2020).
7. T. He, J. Yao, Photochromism in composite and hybrid materials based on transition-metal oxides and polyoxometalates. *Prog. Mater. Sci.* **51**, 810–879 (2006).
8. A. B. A. Kayani *et al.*, UV photochromism in transition metal oxides and hybrid materials. *Small* **17**, e2100621 (2021).
9. G. Ju, Y. Hu, L. Chen, X. Wang, Photochromism of rare earth doped barium haloapatite. *J. Photochem. Photobiol. Chem.* **251**, 100–105 (2013).
10. Y. Badour, V. Jubera, I. Andron, C. Frayret, M. Gaudon, Photochromism in inorganic crystallised compounds. *Opt. Mater. X* **12**, 100110 (2021).
11. Z. Yang, J. Du, L. I. D. J. Martin, D. Van der Heggen, D. Poelman, Highly responsive photochromic ceramics for high-contrast rewritable information displays. *Laser Photonics Rev.* **15**, 1–8 (2021).
12. C. C. Milisenda, S. Koch, S. Müller, T. Stephan, M. Wild, "Gemstones with photochromism" Proceedings, IGC 2015, *Vilnius*, 107–109 (2009).
13. I. Norrbo *et al.*, Mechanisms of tenebrescence and persistent luminescence in synthetic hackmanite Na8Al6Si6O24(Cl,S)2. *ACS Appl. Mater. Interfaces* **8**, 11592–11602 (2016).
14. D. B. Medved, Hackmanite and its tenebrescent properties. *Am. Mineral.* **39**, 615–629 (1954).
15. A. Curutchet, T. Le Bahers, Modeling the photochromism of S-doped sodalites using DFT, TD-DFT, and SAC-CI methods. *Inorg. Chem.* **56**, 414–423 (2017).
16. E. R. Williams, A. Simmonds, J. A. Armstrong, M. T. Weller, Compositional and structural control of tenebrescence. *J. Mater. Chem.* **20**, 10883–10887 (2010).
17. F. Blumentritt *et al.*, Unravelling the origin of the yellow-orange luminescence in natural and synthetic scapolites. *J. Phys. Chem. Lett.* **11**, 4591–4596 (2020).
18. J. A. Armstrong, M. T. Weller, New sodalite frameworks; synthetic tugtupite and a beryllosilicate framework with a 3:1 Si:Be ratio. *Dalt. Trans.* **24**, 2998–3005 (2006).
19. I. Norrbo *et al.*, Solar UV index and UV dose determination with photochromic hackmanites: From the assessment of the fundamental properties to the device. *Mater. Horiz.* **5**, 569–576 (2018).
20. A. Stoliaroff *et al.*, Point defects modeling explains multiple sulfur species in sulfur-doped Na4(Al3Si3 O12)Cl sodalite. *J. Phys. Chem. C* **125**, 16674–16680 (2021).
21. S. B. Lin, B. J. Burley, The crystal structure of an intermediate scapolite - wernerite. *Acta Crystallogr. B* **31**, 1806–1814 (1975).
22. P. Colinet, A. Gheeraert, A. Curutchet, T. Le Bahers, On the spectroscopic modeling of localized defects in sodalites by TD-DFT. *J. Phys. Chem. C* **124**, 8949–8957 (2020).
23. A. Sidike *et al.*, Fine structure in photoluminescence spectrum of S2 — Center in sodalite. *Phys. Chem. Miner.* **34**, 477–484 (2007).
24. J. A. Armstrong, M. T. Weller, Structural observation of photochromism. *Chem. Commun.* **4**, 1094–1096 (2006).
25. X. Wen, D. S. Graham, D. V. Chulhai, J. D. Goodpaster, Absolutely localized projection-based embedding for excited states. *J. Chem. Theory Comput.* **16**, 385–398 (2020).
26. X. Blase, I. Duchemin, D. Jacquemin, The Bethe-Salpeter equation in chemistry: Relations with TD-DFT, applications and challenges. *Chem. Soc. Rev.* **47**, 1022–1043 (2018).
27. S. Vuori *et al.*, Detection of X-ray doses with color-changing hackmanites: Mechanism and application. *Adv. Opt. Mater.* **9**, 2100762 (2021).
28. C. Adamo, V. Barone, Toward reliable density functional methods without adjustable parameters: The PBE0 model. *J. Chem. Phys.* **110**, 6158–6170 (1999).
29. R. Dovesi *et al.*, Quantum-mechanical condensed matter simulations with CRYSTAL. *WIREs Comput Mol Sci.* **8**, 1–36 (2018).
30. R. Nada, J. B. Nicholas, M. I. McCarthy, A. C. Hess, Basis sets for Ab initio periodic hartree-fock studies of zeolite/adsorbate interactions: He, Ne, and Ar in silica sodalite. *Int. J. Quantum Chem.* **60**, 809–820 (1996).
31. R. Demichelis *et al.*, The vibrational spectrum of α-AlOOH diaspore: An ab initio study with the CRYSTAL code. *J. Phys. Chem. B* **111**, 9337–9346 (2007).
32. M. Corno, C. Busco, B. Civalleri, P. Ugliengo, Periodic ab initio study of structural and vibrational features of hexagonal hydroxyapatite Ca10(PO4)6(OH)2. *Phys. Chem. Chem. Phys.* **8**, 2464–2472 (2006).
33. P. C. Hariharan, J. A. Pople, The influence of polarization functions on molecular orbital hydrogenation energies. *Theor. Chim. Acta* **28**, 213–222 (1973).
34. G. Sophia, P. Baranek, C. Sarrazin, M. Rerat, R. Dovesi, Systematic influence of atomic substitution on the phase diagram of ABO3 ferroelectric perovskites. https://www.crystal.unito.it/basis-sets.php. Accessed 28 May 2022.
35. M. J. Frisch *et al.*, Gaussian 16 Revision C.01 (D.J. Gaussian, Wallingford, CT, 2016).
36. A. D. Becke, A new mixing of Hartree-Fock and local density-functional theories. *J. Chem. Phys.* **98**, 1372–1377 (1993).
37. C. Lee, C. Hill, N. Carolina, Development of the Colle-Salvetti correlation-energy formula into a functional of the electron density. *Chem. Phys. Lett.* **162**, 165–169 (1989).
38. S. H. Vosko, L. Wilk, M. Nusair, Accurate spin-dependent electron liquid correlation energies for local spin density calculations: A critical analysis. *Can. J. Phys.* **58**, 1200–1211 (1980).
39. P. J. Stephens, F. J. Devlin, C. F. Chabalowski, M. J. Frisch, Ab Initio calculation of vibrational absorption and circular dichroism spectra using density functional force fields. *J. Phys. Chem.* **98**, 11623–11627 (1994).
40. T. Yanai, D. P. Tew, H. C. Nicholas, A new hybrid exchange-correlation functional using the Coulomb-attenuating method (CAM-B3LYP). *Chem. Phys. Lett.* **393**, 51–57 (2004).
41. M. Klintenberg, S. E. Derenzo, M. J. Weber, Accurate crystal fields for embedded cluster calculations. *Comput. Phys. Commun.* **131**, 120–128 (2000).
42. D. Stueber, F. N. Guenneau, D. M. Grant, The calculation of 13C chemical shielding tensors in ionic compounds utilizing point charge arrays obtained from Ewald lattice sums. *J. Chem. Phys.* **114**, 9236–9243 (2001).
43. S. E. Derenzo, M. K. Klintenberg, M. J. Weber, Determining point charge arrays that produce accurate ionic crystal fields for atomic cluster calculations. *J. Chem. Phys.* **112**, 2074–2081 (2000).